COUPLING OF FREE-BOUNDARY EQUILIBRIUM AND TRANSPORT SOLVERS TO ENABLE MODEL-BASED SCENARIO OPTIMIZATION & INTEGRATED CONTROL

Integrating shape and profile control for advanced scenario development

X. SONG, B. LEARD, Z. WANG, T. RAFIQ, E. SCHUSTER
Lehigh University
Bethlehem, Pennsylvania, USA
Email: xiao.song@lehigh.edu

Abstract

A coupling architecture has been developed to integrate the free-boundary equilibrium (FBE) and transport solvers in COTSIM (Control-Oriented Transport SIMulator). The coupling strategy employs different techniques to make the 2D equilibrium and 1D transport partial differential equations (PDEs) work in a self-consistent way. Sophisticated approaches are employed not only to accelerate the iterations for the FBE solver but also to compensate for deviations in the poloidal flux function at the plasma boundary between the equilibrium and transport solvers. Scaling laws and surrogate models for non-linear current density and heating sources make it possible to calculate transport equations in a fast way. As an illustration of a potential application, a dedicated simulation based on the integrated scheme is performed to study the EAST scenario from ramp-up to flat-top phases. The simulation results demonstrate that self-consistent parameters and profiles are achieved between the equilibrium and transport solvers. The integration of various dimensional solvers within COTSIM makes this platform uniquely qualified for two purposes: firstly, for model-based optimization of advanced scenarios, characterized by specific plasma shapes and core profiles achievable within actuator limits; and secondly, for model-based design and testing of integrated equilibrium and scenario feedback control solutions.

1. INTRODUCTION

The tokamak represents a promising path toward achieving controllable nuclear fusion as a clean and environmentally friendly power source for the grid in the coming decades [1]. In order to enable the ignition condition of fusion in a tokamak reactor, i.e. the triple product of ion temperature (T_i), plasma density (n) and confinement time (τ_e) larger than $3 \times 10^{21} k\text{eV}\cdot m^{-3} \cdot s$, external auxiliary heating sources such as neutral beam injection (NBI), low hybrid wave (LHW) as well as ion or electron cyclotron resonant heating and current drive (I/ECRH and I/ECCD) are needed. Furthermore, in a tokamak reactor, it is essential to simultaneously maintain the plasma current (I_p) and a specific plasma shape, like the X-point configuration. This requires the magnetic field, characterized by toroidal (B_ϕ) and poloidal (B_p) components, induced by external coil currents. This magnetic field configuration is crucial to ensure compatibility with high confinement and to facilitate the exhaust of particles and power from the plasma boundary to plasma wall. Failure to synchronize the control of the auxiliary heating sources and magnetic field in a tokamak reactor can have serious consequences. It not only prevents the plasma from reaching the desired burning state but also increases the risk of off-normal events, such as major disruptions. These events could pose safety challenges for large-scale machines like ITER and FPP, designed for nuclear fusion research.

Reliable integrated simulations of control-oriented plasma scenarios are among the top priorities in the design of the next generation of fusion reactors within the tokamak community. For example, future ITER operations cannot tolerate even a single major disruption [2]. These controls are dominantly categorized into two types, i.e. magnetic control and kinetic control. Magnetic control mainly focuses on the plasma current and plasma shape, from ramp-up (right after the formation of closed magnetic surface) to flat-top and finally to plasma ramp-down phases, where the model is based on the Grad-Shafranov (G-S) equilibrium equation [3]. Whereas the objective of magnetic control is to maintain the specified safety factor (q) profile, e.g., $q_{min} > 1.5$ to avoid certain magnetohyrdodynamics (MHD) modes, and the objective of kinetic control is to reduce transport and produce edge and internal transport barriers in plasma profiles such as electron temperature (T_e) profiles, where an internal electron transport barrier (e-ITB) found on recent EAST campaign to enable one thousand seconds "super" improved mode (I-mode) operation [4]. The calculation of the q-profile relies on the Magnetic Diffusion Equation (MDE) as detailed in [5], while the evolution of electron temperature is determined by the Electron Heat Transport Equation (EHTE) as explained in [6]. Predictive integrated modeling involves the integration of equilibrium, MDE, and transport solvers, along with their associated sources and sinks. This integration enables simulations for the simultaneous application of magnetic and kinetic controls, a task known for its inherent complexity. The complexity of this task primarily arises from dealing with different dimensional aspects. For instance, the free-boundary equilibrium (FBE) involves a 2D problem in (R, Z) coordinates, which requires iterative solutions due to the non-linearity of the toroidal plasma current density in the G-S equation. On the other

hand, the MDE and transport equations are 1D problems, based on the normalized toroidal flux radius ($\hat{\rho}$), and they involve non-linear heating and non-inductive current sources from other complex methods. This is why some current model-based control-oriented simulations tend to focus either on magnetic control with simplified transport coefficient profiles or on kinetic control with simplified equilibrium parameters. Importantly, these integrated simulations rely heavily on intensive calculations performed by integrated modeling codes like TRANSP [7], ASTRA [8], CORSICA [9], JINTRAC [10], and DINA [11]. However, this heavy computational burden often hinders the ability to conduct fast control-oriented scenario designs and developments.

In this study, a fast coupling architecture is developed to integrate the FBE and transport solvers, including MDE. This architecture is designed for model-based, control-oriented simulations focused on EAST. The coupling process involves the exchange of profiles and parameters between the equilibrium and transport solvers. To address deviations in the boundary poloidal flux function between the FBE and MDE, flux components decoupled from coils currents are used to offset these discrepancies. The transport equations have been efficiently solved using COTSIM's library of models, which encompass various complexities designed to suit different control applications. These models include analytical, scaling laws, empirical, and neural network models trained from physics-based codes. Finally, the integrated scheme is applied to study the EAST scenario from ramp-up to flat-top phases, demonstrating self-consistent results between the FBE and transport solvers. The organization of this paper is as follows. Section 2 presents the equilibrium and transport equations and their couplings. The simulation of ramp-up to flat-top for the EAST scenario using the coupling scheme is detailed in Section 3. In Section 4, the conclusion is provided, and potential future work is outlined.

2. EQUATIONS FOR EQUILIBRIUM AND TRANSPORT AND THEIR COUPLINGS

A synthetic model based on the FBE and transport equations is needed to develop the control algorithm for integrated magnetic and kinetic controls. The solvers to calculate those PDEs with different dimensions in a fast way should use similar numerical methods within certain computational environments. More importantly, this synthetic model must contain the necessary physical issues, including inductive I_p consumption, vertical displacement events (VDEs), ITB, and pedestal properties.

2.1. G-S Equilibrium Equation

Because of the toroidally axisymmetric assumption in tokamak geometry, only the cylindrical coordinate system consisting of (R, Z) is taken into account. The G-S equation for the FBE problem, which is derived from the force balance equation, is expressed as stated in [12].

$$\Delta^* \psi(R,Z) \quad = -\mu_0 R J_\phi(R,Z), \tag{1a}$$

$$\Delta^* \quad \equiv R\tfrac{\partial}{\partial R}\big(\tfrac{1}{R}\tfrac{\partial}{\partial R}\big) + \tfrac{\partial^2}{\partial Z^2}. \tag{1b}$$

The poloidal flux function ψ, which represents the poloidal magnetic flux per radian, is defined as $\psi(R,Z) \equiv RA_\phi$ based on the equation $B = \nabla \times A$ (with $\nabla \cdot B = 0$). Here, μ_0 represents the permeability in a vacuum region. The term $J_\phi(R,Z)$ in (1a) represents the toroidal current density and varies depending on different regions.

$$J_\phi(R,Z) = \begin{cases} Rp'(\psi) + \frac{ff'(\psi)}{\mu_0 R} & \text{in plasma area } \Omega_{pl} \\ \frac{I_i}{S_i} & \text{in coil number } i \\ 0 & \text{elsewhere} \end{cases} \tag{2}$$

Here p represents plasma kinetic pressure, f is the diamagnetic function defined as $f(\psi) \equiv RB_\phi$, and I_i and S_i denote the current and cross-section of external conductor coil i, both p and f are functions dependent on ψ. It is beneficial to introduce the normalized poloidal flux function, denoted as $\psi_N = (\psi - \psi_{ax})/(\psi_{bd} - \psi_{ax})$, ensuring it ranges from 0 at the magnetic axis (ψ_{ax}) to 1 at the plasma boundary (ψ_{bd}). It is worth noting that a similar approach can be applied to calculate the toroidal current density (J_ϕ) induced on passive plates and the vacuum vessel due to plasma vertical excursions or disruptions, akin to the treatment of J_ϕ in external coils. To expedite the execution of the FBE solver, we use the equilibrium results from previous runs, including coil currents and the ψ map, as the initial guess for the next FBE calculation.

Recently, a numerical solver based on the finite difference method (FDM) with Picard iteration has been developed for solving the FBE problem [13]. This solver operates within a Matlab/Simulink environment[1] and can run in either direct mode, where external coil currents are prescribed, or inverse mode, where the targeted plasma boundary, with or without an X-point, is pre-specified to find the required coil currents. The boundary condition for this solver is defined as

$$\mathbf{B.C.}: \psi_{grid,bd}\,(R_{bd}, Z_{bd}) = \int_{\Omega_{pl}} G(R_{bd}, Z_{bd}; R'', Z'') J_{\phi,pl}(R'', Z'')\, dR'' dZ'' + \sum_{i=1}^{N_{\text{coil}}} G(R_{bd}, Z_{bd}; R_i, Z_i) \cdot I_i \tag{3}$$

[1] *www.mathworks.com*

where R_{bd}, Z_{bd} are boundary points of the computational mesh, G is the Green's function, (R'', Z'') and (R_i, Z_i) are the mesh points (except those on mesh boundary) and coordinates of coils areas, respectively.
In this work, the objective of inverse mode with targeted plasma separatrix (R_j^{ref}, Z_j^{ref}) is considered by

$$\underset{\Delta I_{\text{coil}}}{min}\left[\sum_{j=1}^{N_{\text{bnd}}}\left\{\sum_{i=1}^{N_{\text{coil}}}\left(G\Big(R_j^{ref}, Z_j^{ref}; R_i, Z_i\Big)\cdot\Delta I_{coil,i}\right)-\Delta\psi\Big(R_j^{ref}, Z_j^{ref}\Big)\right\}^2+\gamma^2\sum_{i=1}^{N_{\text{coil}}}\Big(\Delta I_{coil,i}\Big)^2\right] \tag{4}$$

in which $\Delta\psi(R_j^{ref}, Z_j^{ref}) = \psi_{bd} - \psi(R_j^{ref}, Z_j^{ref})$ is the error of poloidal flux on prescribed plasma boundary points (R_j^{ref}, Z_j^{ref}), γ is a Tikhonov parameter for regularization term in an ill-posed problem [14].

2.2. Magnetic Diffusion Equation

Unlike the FBE, which is determined in terms of (R, Z) coordinates, the transport equations are performed using the effective minor radius, ρ, with the toroidal flux, Φ.

$$\Phi \equiv \pi B_0 \rho^2 \ \ , \ \ \rho_b \equiv \sqrt{\frac{\Phi_b}{\pi B_0}} \ \ , \ \ \hat{\rho} \equiv \frac{\rho}{\rho_b} \in [0,1], \tag{5}$$

where, Φ_b represents Φ at the plasma boundary, B_0 is the toroidal magnetic field at the major radius R_0, $\hat{\rho}$ is the normalized effective minor radius, and ρ_b is the effective minor radius at the plasma boundary.
The MDE and its boundary conditions are defined as follows

$$\frac{\partial\psi}{\partial t} = \frac{\eta(T_e)}{\mu_0\rho_b^2F^2}\frac{1}{\hat{\rho}}\frac{\partial}{\partial\hat{\rho}}\Big(\hat{\rho}FGH\frac{\partial\psi}{\partial\hat{\rho}}\Big)+\frac{R_0H\eta(T_e)}{B_0}\langle j_{NI}\cdot B\rangle \tag{6a}$$

$$\mathbf{B.C.}: \frac{\partial\psi}{\partial\hat{\rho}}\Big|_{\hat{\rho}=0} = 0;\ \frac{\partial\psi}{\partial\hat{\rho}}\Big|_{\hat{\rho}=1}^{t} = -\frac{\mu_0R_0}{2\pi GH}I_p(t). \tag{6b}$$

Here, $\eta(T_e)$ represents plasma resistivity, which is dependent on the electron temperature T_e, and j_{NI} stands for non-inductive plasma current, encompassing contributions from bootstrap and auxiliary current drive methods such as E/ICCD, LHCD, and NBCD. The flux-averaged $< \cdot >$ quantities F, G, and H are equilibrium parameters that are defined as follows.

$$F = \frac{R_0B_0}{f}\ ,\ G = \langle\frac{R_0^2|\nabla\rho|^2}{R^2}\rangle\ ,\ H = \frac{F}{\langle R_0^2/R^2\rangle} \tag{7}$$

The transport equation solvers in COTSIM [15] utilize FDM within the Matlab/Simulink environment, a widely adopted platform for control design across development stages. COTSIM provides an extensive library of models with varying complexities to suit diverse control applications, including analytical models, scaling laws, empirical models, and neural-network models trained from physics-based codes [16].

2.3. Coupling Between Free Boundary Equilibrium and Transport Solvers

The scheme, as illustrated in Fig.1, designed to couple the 2D FBE and 1D transport solvers, is achieved by reducing the 2D (R, Z) FBE into a 1D equation based on ψ_N. With the initial transport profiles, the equilibrium (1) is solved by computing the right-hand side of J_ϕ, which is a function of $p'(\psi_N)$ and $ff'(\psi_N)$ [17], derived from ψ, T_i, T_e, n_i, n_e. Initial equilibrium parameters in terms of F, G, H must be provided to calculate $p'(\psi_N)$ and $ff'(\psi_N)$, as defined by

$$p'(\psi_N) = \frac{\partial p}{\partial\hat{\rho}}\frac{\partial\hat{\rho}}{\partial\psi_N} = k_B\frac{\partial(n_e\cdot T_e + n_i\cdot T_i)}{\partial\hat{\rho}}\frac{\partial\hat{\rho}}{\partial\psi_N}\ ;\ ff'(\psi_N) = -\frac{1}{\left\langle\frac{1}{R^2}\right\rangle}\left(\frac{\partial\hat{\rho}}{\partial V}\frac{\partial}{\partial\hat{\rho}}\Big(\frac{\partial\psi}{\partial\hat{\rho}}\cdot\frac{\partial V}{\partial\hat{\rho}}\frac{G}{R_0^2\rho_b^2}\Big)+\mu_0p'(\psi_N)\right), \tag{8}$$

where k_B represents the Boltzmann constant and V signifies the plasma volume. After solving the FBE, which yields a new equilibrium configuration represented by flux-averaged quantities, this configuration is then passed to the transport solvers for the next time step.
The boundary condition for this coupling requires that the ψ values at the plasma boundary, as predicted by both solvers, should be self-consistent. In other words, $\psi^{Eq}_{\psi_N=1}$ should match $\psi^{Tr}_{\hat{\rho}=1}$ when both equilibrium and transport solvers are converged. Any deviations in ψ between the FBE and MDE can be compensated by adjusting a set of coil currents referred to as IPF_{Ohm}. These currents are computed through a minimization process $\sum_{k=1}^{n}\left(1 - G(R_k, Z_k, R_{coils}, Z_{coils})\text{IPF}\right)^2$. Here, (R_k, Z_k) represents mesh points within the plasma region [18]. IPF_{Ohm} contributes solely to the ψ value without affecting the plasma shape (i.e., no B_p contribution), maintaining constant ψ values across all plasma nodes for inductive consumption. Finally, the total coil currents for scenario development are determined as the sum of IPF_{Shp} obtained from the inverse mode of FBE and IPF_{Ohm}, i.e., IPF = $a\text{IPF}_{\text{Ohm}}$ + IPF_{Shp}, where the scaling factor a adjusts for the deviation in boundary ψ between the equilibrium and transport solvers.

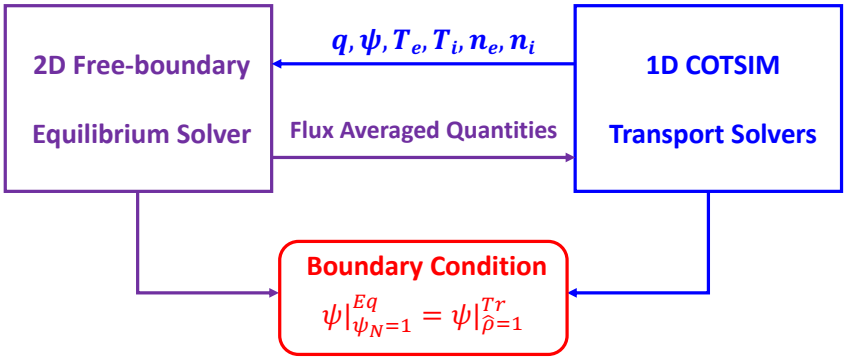

FIG. 1. Coupling scheme between the equilibrium and transport solvers.

3. SIMULATION FROM RAMP-UP TO FLAT-TOP PHASES

While it is essential to assess stable equilibrium states and transport profiles at flat-top, the simulation of the ramp-up phase and its transition to flat-top is even more crucial, albeit more challenging, for developing realistic plasma scenarios. During ramp-up, various key parameters such as J_ϕ, q, T_e, and n_e, as well as plasma equilibrium parameters, undergo significant and intricate interactions, potentially leading to disturbances and instabilities. For this reason, it is of utmost importance to comprehensively assess the dynamics between equilibrium and transport properties from the ramp-up to the flat-top phase using an integrated scheme. Such an approach provides invaluable insights necessary for designing control-oriented strategies and advanced scenarios to effectively schedule the whole machine operation. In this work, the EHTE and its boundary conditions are written as

$$\frac{3}{2}\frac{\partial}{\partial t}\left(n_e T_e\right) = \frac{1}{\rho_b^2 H}\frac{1}{\hat{\rho}}\frac{\partial}{\partial \hat{\rho}}\left[\hat{\rho}\frac{GH^2}{F}\left(\chi_e(\cdot) n_e \frac{\partial T_e}{\partial \hat{\rho}}\right)\right] + Q_e\text{-dep} \tag{9a}$$

$$\mathbf{B.C.}: \left.\frac{\partial T_e}{\partial \hat{\rho}}\right|_{\hat{\rho}=0} = 0;\ \left. T_e\right|^t_{\hat{\rho}=1} = T_e^{bdry}(t). \tag{9b}$$

Here, thermal diffusivity (χ_e) and the total power density deposited into electrons (Q_e-dep) play crucial roles. Notably, our approach assumes equal electron and ion temperatures ($T_e = T_i$) and does not incorporate an ion heat transport equation. Additionally, the electron density profile (n_e) is determined by the line-averaged electron density ($\overline{n}_e$).

$$n_e(\hat{\rho}, t) = n_e^{prof}\overline{n}_e(t), \tag{10}$$

where n_e^{prof} is typically read from experiment.

3.1. Simulation Settings

Simulations were conducted using the coupling scheme, with settings derived from experimental data obtained during the EAST pulse. The plasma current (I_p) ramp-up rate was set to 0.15 MA/s, and the fraction of the Greenward limit (f_g) for the line-averaged electron density ($\overline{n}_e$) was kept constant at 0.7 throughout the entire simulation. Power inputs of 2 MW for PLH and 1 MW for PNBI were employed. The prescribed plasma boundary was determined from experimental data, and detailed parameters are provided in Table 1. The simulation covered a 1-second ramp-up phase and a 1-second flat-top phase, with 0.1-second intervals. A visual representation of the prescribed settings and the trajectory of the plasma boundary can be found in Fig. 2. Four vertical dashed lines therein indicate the locations of various profiles obtained from equilibrium and transport results at different time steps, which are presented in subsequent subsections.

TABLE 1. PLASMA BOUNDARY PARAMETERS

R_0 (m)	a (m)	κ	δ	(R^{Xpt} , Z^{Xpt}) (m , m)	B_0 (T)
1.8	0.45	1.42	0.5	(1.66 , -0.88)	2.5

3.2. Evolution of Equilibrium Quantities

The calculation of the FBE equation constitutes the most time-consuming aspect of the coupling process because the solver relies entirely on iterations. As introduced in Section 2.3, a scheme enables all subsequent time evolution FBE solvers, except

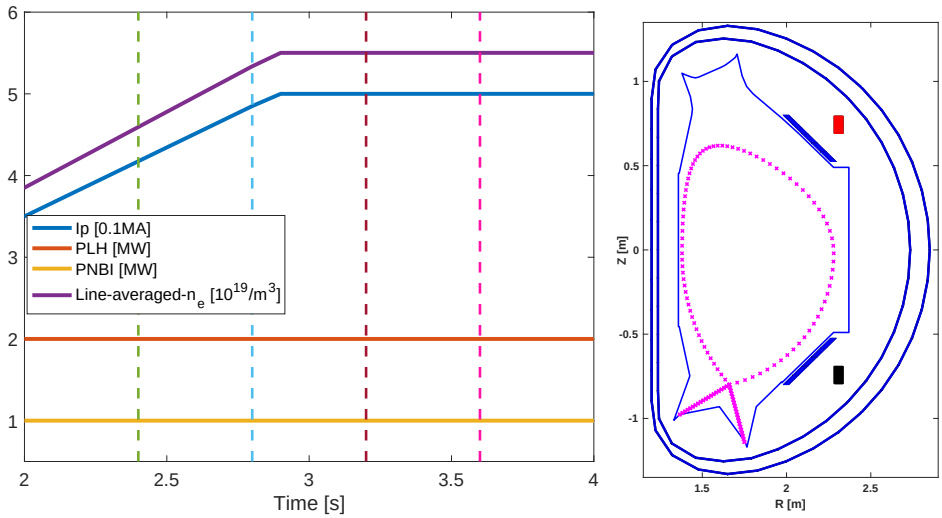

FIG. 2. Prescribed trajectories of I_p, PLH, PNBI and $\overline{n}_e$, (left) and plasma boundary (right) for ramp-up to flat-top integrated simulation.

for the initial one, to converge in less than 20 iterations with a tolerance of 10^{-2}, whereas the initial solver may require approximately 60 to 70 iterations before reaching convergence.

The decision to use the same prescribed plasma boundary in the inverse FBE solver is primarily driven by the need to calculate $\mathrm{IPF_{Ohm}}$. When there are changes in the plasma shape, it leads to corresponding variations in $\mathrm{IPF_{Ohm}}$, making it challenging to offset the deviation of ψ_{bd} between the equilibrium and transport solvers effectively. It is important to emphasize that maintaining the constraint $\mathrm{IPF_{Ohm}^{T}}\cdot\mathrm{IPF_{Shp}} = 0$ is crucial. This constraint must be satisfied to minimize coupling with the plasma current drive performed by $\mathrm{IPF_{Ohm}}$ [18].

Figure 3 presents the evolution of the plasma boundary at selected time steps, along with the coil currents obtained from the FBE solver, where J_ϕ is determined by the transport solvers. Notably, the plasma boundaries are effectively maintained by the inverse mode of the FBE solver, as indicated in the reference shown in the right panel of Fig. 2. In the context of coil currents, the dominant components of $\mathrm{IPF_{Ohm}}$, specifically the currents in coils PF1 to PF6, are reduced to provide energy for inductive plasma current consumption (I_p). Conversely, the remaining currents in coils PF7 to PF14, which constitute the primary components of $\mathrm{IPF_{Shp}}$, responsible for generating the necessary vertical magnetic field to maintain equilibrium, remain nearly constant. Additionally, it is worth noting that coils PF6, PF8, and PF10 exhibit substantial currents, as they play a critical role in sustaining the X-point.

3.3. Evolution of Transport Profiles

The transport equations, described in terms of MDE and EHTE, are efficiently solved in COTSIM by utilizing scaling laws. These scaling laws involve fixed profiles for non-inductive current density and power deposition, which are derived from experimental data [19]. To initiate the transport solvers, the initial equilibrium quantities, such as F, G, and H, are provided by an inverse FBE solver, where the J_ϕ is parameterized using polynomials based on ψ_N [20].

Fig.4 displays selected profiles from the transport solvers associated with time-evolving equilibrium quantities. In COTSIM, j_{LHCD} and j_{NBCD} depend on (T_e/n_e) $(P_{\mathrm{LH}}, P_{\mathrm{NB}})$, respectively. Consequently, during the ramp-up phase (blue and cyan), j_{LHCD} and j_{NBCD} are higher due to the elevated T_e/n_e compared to the flat-top phase (purple and magenta), as observed in the top-left plot of Fig.4. This indicates that more injected power or lower n_e is required to maintain a high fraction of non-inductive I_p during the flat-top phase.

Conversely, in the bottom-left plot of Fig.4, we observe that the total deposited power density, Q_e-dep, which encompasses both Ohmic and auxiliary contributions, is reduced during the ramp-up phase. This reduction is primarily attributed to a decrease in the Ohmic power component, driven by the smaller value of η during this phase. Meanwhile, the auxiliary power remains constant. As a result, this reduction in power deposition leads to a lower p profile $(T_e \cdot n_e)$, as illustrated in the left plot of Fig.6. For the calculation of χ_e, this work employs the 1D Coppi-Tang transport model [21]. The similarity in χ_e values observed at different time steps implies that changes in electron heat transport will likely have a minimal effect on profile variations.

3.4. Cross-checking of Parameters and Profiles Between Equilibrium and Transport Solvers

The validation of parameters and profiles across the FBE, MDE, and EHTE solvers plays a crucial role in the coupling process. It is important to note that deviations in profiles can occur, particularly in regions near the plasma axis and boundary. This is

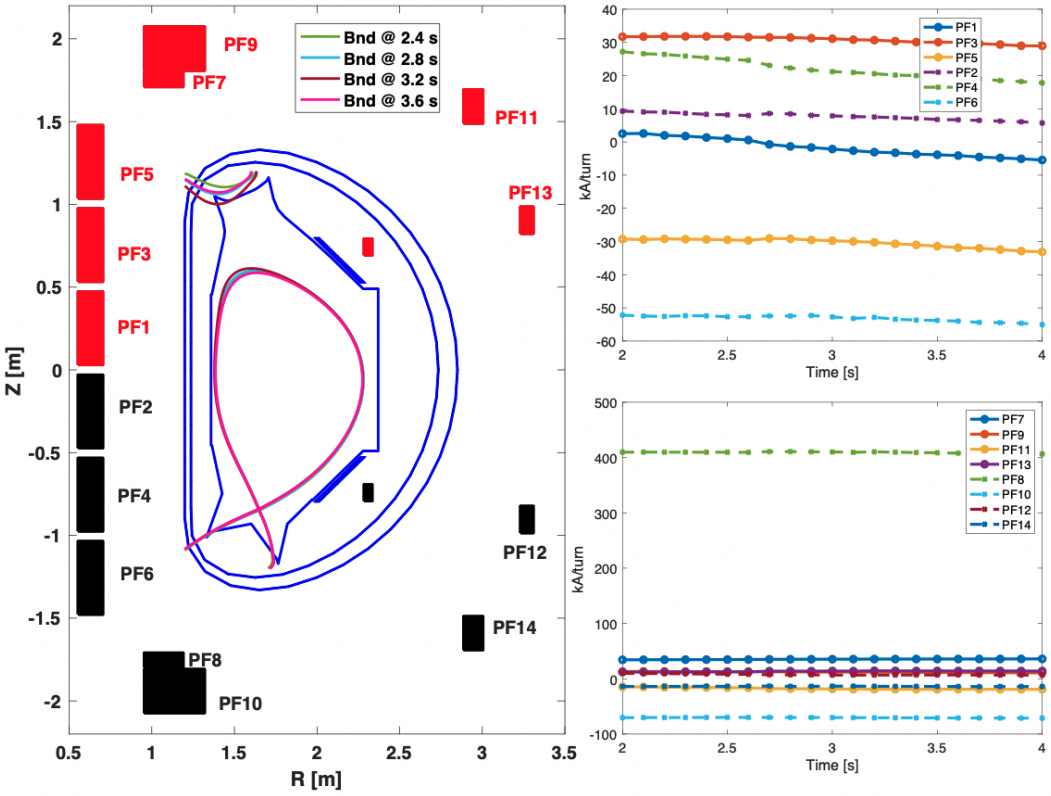

FIG. 3. Selected evolutions of plasma boundaries (left) and coil currents (right).

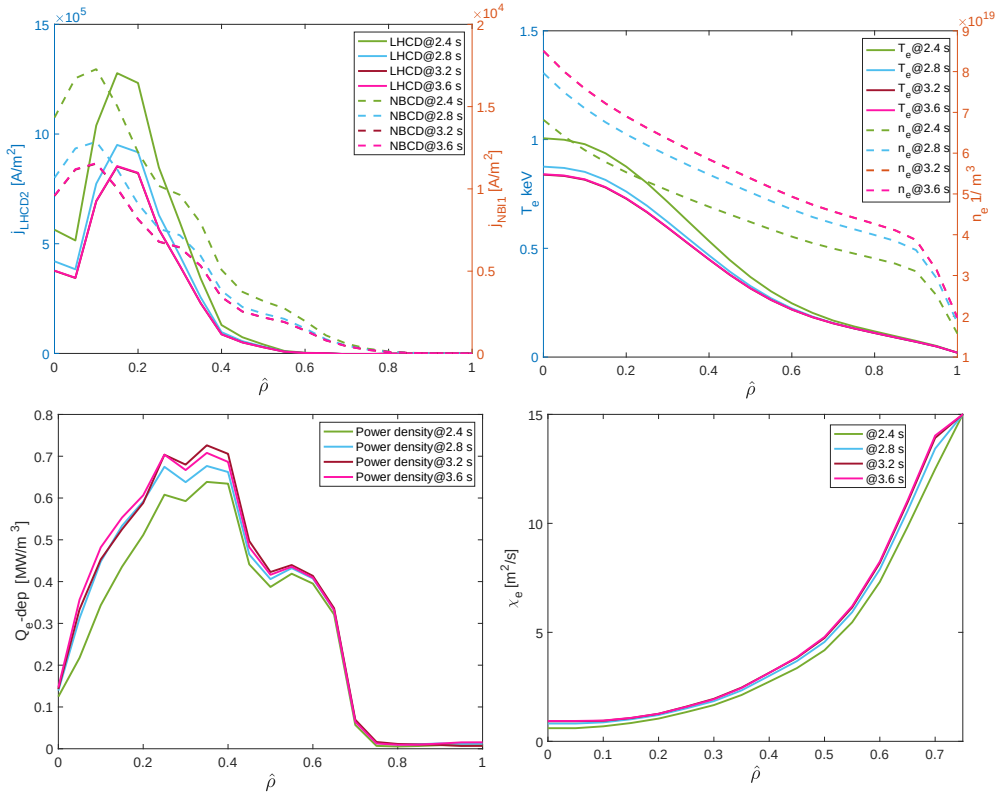

FIG. 4. Evolution of non-inductive j_{LHCD}, j_{NBCD} (upper left panel), T_e, and n_e (upper right panel), along with power density deposition on electrons (lower left panel) and χ_e (lower right panel).

due to the requirement for a smooth J_ϕ profile in the FBE solver and potential numerical errors resulting from approximations with FDM at $\hat{\rho} = 0$ and $\hat{\rho} = 1$.

Fig.5 displays the selected q and θ values. It is evident that q values are well-matched for $\hat{\rho} < 0.4$, but a noticeable deviation emerges from $\hat{\rho} = 0.4$ to the plasma boundary. This deviation aligns with the differences in θ values, as depicted in the right panel of Fig.5. While the deviation in ψ_{bd} between FBE and MDE is compensated for as described in Section 2.3, it is worth noting that the ψ value at $\psi_N = 0$ is unconstrained in the FBE solver, whereas the θ value at $\hat{\rho} = 0$ for the transport solver is fixed at 0. This highlights the importance of deriving the targeted q_{95} from MDE rather than the FBE solver, as the latter may potentially lose essential information at $\psi_N = 1$ under specific circumstances, such as the pedestal with high confinement mode (H mode).

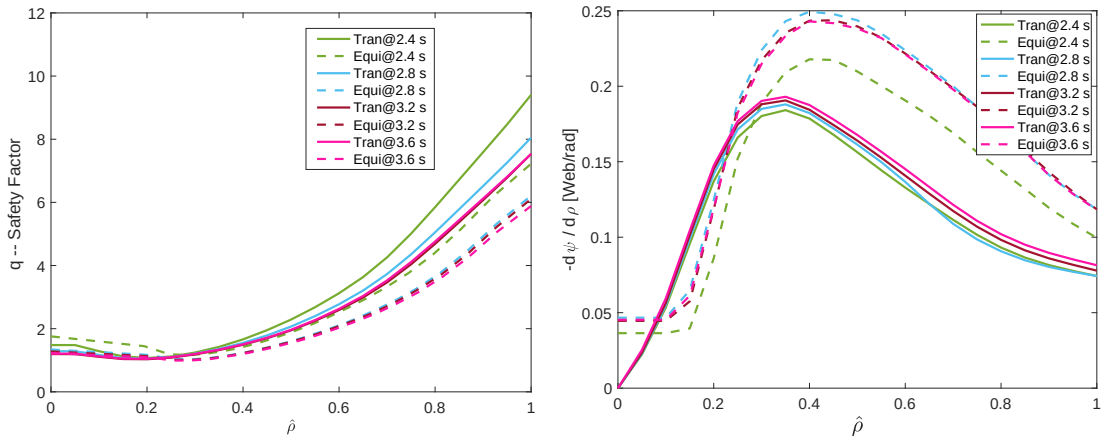

FIG. 5. Evolution of q (left) and θ, i.e., $-\frac{d\psi}{d\hat{\rho}}$ (right), compared between FBE and transport solvers.

Fig. 6 provides the selected p profiles for the FBE, MDE, and EHTE solvers. The inconsistencies observed in the p profiles between the FBE and transport solvers are likely attributed to the smoothed $p'(\psi_N)$ in J_ϕ. This smoothed $p'(\psi_N)$ is essential to ensure stable convergence during iterations in the FBE solver, particularly at the plasma axis and boundary. To address this limitation, future work may explore options such as refining the mesh, although this would increase computational time. It is clear that more approaches should be investigated to effectively manage these challenges. The Shafranov shift, represented by β_p+$l_i/2$, is shown in the right panel of Fig.6. The similarity in β_p+$l_i/2$ values indicates that deviations in profiles and global parameters between the equilibrium and transport solvers are minimal, particularly during the ramp-up phase from 2 seconds to 3 seconds, as evident in Fig.6.

The alignment of parameters and profiles between the equilibrium and transport solvers signifies the successful integration of magnetic and kinetic controls. This integration demonstrates self-consistent simulations from the ramp-up to flat-top phases for EAST, with exceptions occurring primarily near $\hat{\rho} = 0$ and $\hat{\rho} = 1$ due to sharp profile changes resulting from FDM approximations. Moreover, this fast integrated simulation holds promise not only for scenario development but also for experimental analysis during the interval between two shots. It offers versatility and practicality in both simulation and experimental contexts.

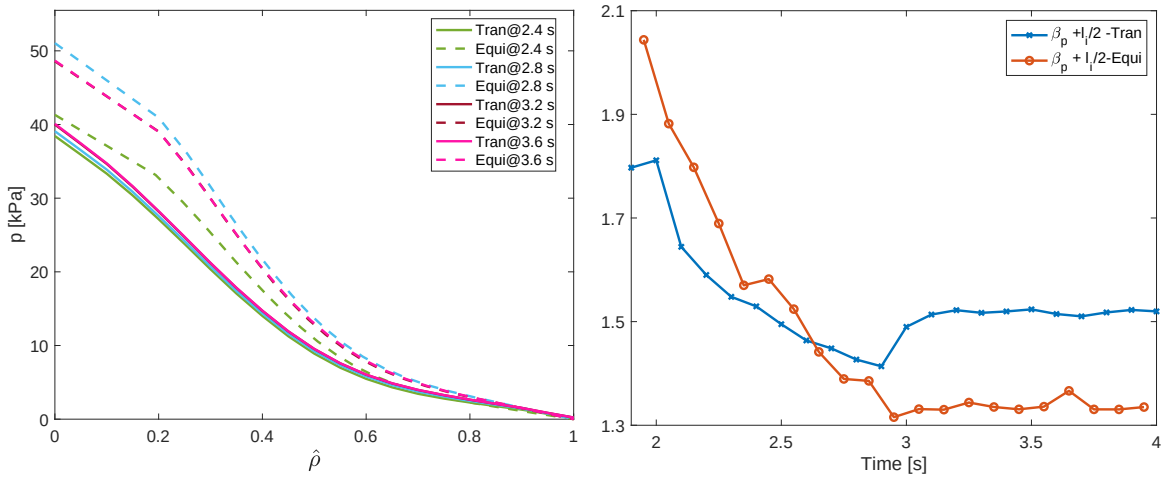

FIG. 6. Evolution of p (left) and β_p + $l_i/2$ (right) compared between FBE and transport solvers.

4. CONCLUSION AND FUTURE WORK

In this study, an integrated architecture has been developed in COTSIM by coupling 2D FBE and 1D transport solvers (in terms of MDE and EHTE). Simulations with plasma dynamics between equilibrium and transport properties can be run in just a few minutes using this coupling scheme. FDM with boundary conditions is employed by all the FBE and transport solvers to solve the PDEs within the Matlab environment, a platform broadly used for control design at all stages of development. The boundary condition for combining the 2D FBE and 1D transport solvers ensures self-consistency of ψ at the plasma boundary, where possible deviations can be easily offset by IPF_{Ohm} through a certain set of coil currents. The EAST scenario, covering the ramp-up to flat-top phases with 2 MW LHCD and 1 MW NBI heating and current drive, is studied using this integrated scheme. The simulation is analyzed by benchmarks on parameters and profiles from both the equilibrium and transport solvers. Self-consistent parameters and profiles are found by coupling solvers with different dimensions, enabling magnetic and profile controls to be synthetically enabled for the design of future reactors such as ITER and FPP.

The coupling process relies on intensive calculations with iterations to solve the equilibrium equation. Therefore, there is a high demand for surrogate approaches, such as neural networks, in the next steps to accelerate the FBE solver. Additionally, embedding circuit equations and models for the vacuum vessel and passive plates within the FBE solver would enable the use of coil voltages as actuators for magnetic control. To further enhance the integrated scheme's capabilities, it is essential to replace fixed profiles with time evolution models for non-inductive current density and heating sources. This expansion allows for more comprehensive physics considerations. Lastly, developing closed-loop simulations with various scales of feedback control laws for both slow magnetic control and fast kinetic control, utilizing available actuators like coil voltages and different heating and fueling sources, holds significant value.

ACKNOWLEDGEMENTS

This material is based upon work supported by the U.S. Department of Energy, Office of Science, Office of Fusion Energy Sciences under Award DE-SC0010537.

REFERENCES

[1] ZOHM, H., *Philosophical Transactions of the Royal Society A* **377** (2019) 20170437.

[2] DE VRIES, P. C., LUCE, T. C., BAE, Y., et al., *Nucl. Fusion* **58** (2017) 026019.

[3] SHAFRANOV, V., *Sov. Phys. JETP* **8** (1958) 494.

[4] SONG, Y., ZOU, X., GONG, X., et al., *Sci. Adv.* **9** (2023) eabq5273.

[5] OU, Y., XU, C., SCHUSTER, E., et al., *Plasma Phys. Control. Fusion* **50** (2008) 115001.

[6] RAFIQ, T., KRITZ, A., WEILAND, J., PANKIN, A., and LUO, L., *Phys. Plasmas* **20** (2013).

[7] HAWRYLUK, R., An empirical approach to tokamak transport, in Physics of plasmas close to thermonuclear conditions, pp. 19–46, Elsevier, 1981.

[8] PEREVERZEV, G. V. and YUSHMANOV, P., ASTRA automated system for transport analysis in a Tokamak, IPP-Report 5/98 Max-Planck-Institut fur Plasmaphysik (2002).

[9] CROTINGER, J. A., LLNL Report UCRL ID 126284, NTIS PB2005-102154 (1997).

[10] ROMANELLI, M., CORRIGAN, G., PARAIL, V., et al., *Plasma and Fusion research* **9** (2014) 3403023.

[11] KHAYRUTDINOV, R. and LUKASH, V., *J. Comput. Phys.* **109** (1993) 193.

[12] GRAD, H. and RUBIN, H., Proceedings of the second united nations international conference on the peaceful uses of atomic energy, 1958.

[13] SONG, X., LEARD, B., and SCHUSTER, E., *Bulletin of the American Physical Society* (2022).

[14] TIKHONOV, A. N. and ARSENIN, V., *Solutions of ill-posed problems* (1977).

[15] PAJARES, A., *Integrated Control in Tokamaks using Nonlinear Robust Techniques and Actuator Sharing Strategies*, PhD thesis, Lehigh University, 2019.

[16] MOROSOHK, S., PAJARES, A., RAFIQ, T., and SCHUSTER, E., *Nucl. Fusion* **61** (2021) 106040.

[17] GARCIA-MARTINEZ, P. L. and MONTES, P., *Fusion Eng. Des.* **152** (2020) 111455.

[18] WALKER, M. L., LANCTOT, M. J., and HAHN, S.-H., Online feedforward calculation for plasma shape control in tokamaks with superconducting coils, in 2016 IEEE Conference on Control Applications (CCA), pp. 605–610, IEEE, 2016.

[19] WANG, Z., SCHUSTER, E., RAFIQ, T., et al., *Bulletin of the American Physical Society* (2021).

[20] JEON, Y. M., *J. Korean Phy. Soc.* **67** (2015) 843.

[21] JARDIN, S. C., BELL, M., and POMPHREY, N., *Nucl. Fusion* **33** (1993) 371.